Suppression of Resistive Coupling in Nanogap Electrochemical Cell: Resolution of Dual Pathways for Dopamine Oxidation

Amir Amiri,[†] Manu Jyothi Ravi,[†] Siao-Han Huang, Donald C. Janda, and Shigeru Amemiya*

Department of Chemistry, University of Pittsburgh, 219 Parkman Avenue, Pittsburgh, Pennsylvania, 15260, United States

[†] These authors contributed equally to this work.

* To whom all correspondence should be addressed. E-mail: amemiya@pitt.edu.

Abstract

A nanogap cell involves two working electrodes separated by a nanometer-wide solution to enable unprecedented electrochemical measurements. The powerful nanogap measurements, however, can be seriously interfered with by resistive coupling between the two electrodes to yield erroneous current responses. Herein, we employ the nanogap cell based on double carbon-fiber microelectrodes to suppress resistive coupling for the assessment of intrinsic current responses. Specifically, we modify a commercial bipotentiostat to compensate the Ohmic potential drop shared by the two electrodes through the common current pathway with a fixed resistance in the solution. Resistive coupling through both non-Faradaic and Faradaic processes is suppressed to eliminate erroneous current responses. Our approach is applied to investigate the mechanism of dopamine oxidation at carbon-fiber microelectrodes as important electrochemical sensors for the crucial neurotransmitter. Resistive coupling is suppressed to manifest the intrinsic current responses based on the oxidation of both adsorbed and non-adsorbed forms of dopamine to the respective forms of dopamine-*o*-quinone. The simultaneous dual oxidation pathways are observed for the first time and can be mediated through either non-concerted or concerted mechanisms of adsorption-coupled electron transfer. The two mechanisms are not discriminated for the two-electron oxidation of dopamine because it can not be determined whether the intermediate, dopamine semi-quinone, is adsorbed on the electrode surface. Significantly, our approach will be useful to manifest intrinsic current responses without resistive coupling for nanogaps and microgaps, which are too narrow to eliminate the common solution resistance by optimizing the position of a reference electrode.

Keywords

Nanogap electrochemical cell

Resistive coupling

Carbon fiber microelectrode

Dopamine

Adsorption-coupled electron transfer

Ohmic potential drop

1. Introduction

Two working electrodes are separated by a nanometer-wide solution to constitute a nanogap electrochemical cell as an unprecedentedly powerful electroanalytical method [1]. Technological advancements have been made to form nanogap cells based on nanoscale scanning electrochemical microscopy (SECM) [2, 3] or nanolithography and nanofabrication [4, 5]. With either approach, a redox-active species in the nanogap is electrolyzed at the generator electrode and regenerated at the collector electrode to mediate redox cycling (or diffusional crosstalk). The highly efficient diffusion of the redox couple across the nanogap largely enhances the Faradaic current at both electrodes, which is attractive for sensitive electrochemical analysis [6]. Moreover, the electrochemical detection of single molecules [7-9] and single nanoparticles [10, 11] is enabled by nanogap cells, where the individual entities are trapped to produce current blips. Nanogap cells also allow for kinetic studies of faster electron-transfer [12, 13] and chemical [14, 15] reactions than microgap cells. Advantageously, the diffusional crosstalk across a nanogap can be maintained voltammetrically at scan rates of even 100 V/s [16, 17] for fast electrochemical sensing [18] and the resolution of adsorption-coupled electron-transfer mechanisms [19].

Herein, we reveal the intrinsic current responses of double carbon fiber microelectrodes (CFMs) (Figure 1A) as an emerging nanogap-based sensor [18, 20] by suppressing resistive coupling between the two electrodes. Previous studies of nanogap cells assessed capacitive coupling [10, 21, 22] but not resistive coupling, which distorts the current responses of millimeter-gap [23-29] and micrometer-gap [30-33] cells. With any gap width, the potentials of generator and collector electrodes, E_G and E_C, respectively, are controlled independently against a reference electrode to measure the current responses of the respective electrodes, i_G and i_C. These electrodes, however, are coupled resistively by sharing a current pathway with a fixed resistance, R_S, in the solution (Figure 1B), thereby developing a common Ohmic potential drop, $(i_G + i_C)R_S$. The potential of each working electrode against the reference

electrode involves the common Ohmic potential drop, which varies with the current response of the other working electrode. Problematically, a change in the current response of one working electrode affects the potential drop across the interface between the other working electrode and the solution to induce the erroneous current response of the latter electrode.

In this work, we manifest the intrinsic current response of the amperometric collector electrode without resistive coupling with the voltammetric generator electrode by compensating the common Ohmic potential drop. This approach was successfully applied for rotating ring disk electrodes (RRDEs) with millimeter gaps by Shabrang and Bruckenstein [26] but has never been applied to nanogap [18] or microgap [30-33] cells. Specifically, we modify a commercial bipotentiostat to compensate the potential of the collector electrode, E_C, by the common Ohmic potential drop based on the generator current, $i_G R_S$, instead of the collector current, $i_C R_S$, as practiced without the modification [34]. We suppress resistive coupling not only through non-Faradaic processes [31] but also through Faradaic processes [23-29]. The latter is also known as the pseudocollection effect [24, 25]. An alternative approach to the suppression of resistive coupling is to minimize the common solution resistance, R_S, by optimizing the position of a reference electrode against an RDDE [23-29], which uses a Luggin capillary. This approach is not applicable for narrow microgap and nanogap cells, where resistive coupling has not been suppressed [18, 30-33].

Significantly, we applied our approach to better understand the mechanism of dopamine (DA) oxidation at CFMs as a widely used electrochemical sensor for this imperative neurotransmitter [35]. Previously, we employed double CFMs to oxidize DA at the generator electrode by fast-scan cyclic voltammetry and detect the product of two-electron transfer, dopamine-*o*-quinone (DOQ), at the amperometric collector electrode [18]. The collector response, however, was seriously distorted by the current peaks that were not expected from voltammetric theory [17]. In this work, the distorting current

peaks are attributed to resistive coupling and suppressed experimentally to demonstrate that a CFM oxidizes both adsorbed and non-adsorbed forms of DA simultaneously. The dual oxidation pathways were proposed previously [36] but have not been observed separately. Moreover, we find that each oxidation pathway can be mediated through either a non-concerted or concerted mechanism. This ambiguity was unexpected because DA oxidation satisfies two requirements proposed for voltammetric discrimination between the two mechanisms of one-electron transfer [37, 38]. Two-electron-transfer reactions also require the identification of the adsorbed or non-adsorbed intermediate, i.e., dopamine sei-quinone (DSQ), on the collector electrode to determine a concerted or non-concerted mechanism, respectively.

2. Model

2.1. Assumptions

We employ the equivalent circuit (Figure 1B) to model the resistively coupled current responses of voltammetric generator and amperometric collector electrodes. Similar equivalent circuits were employed successfully to model the resistive coupling of non-Faradaic currents for SECM [31] or Faradaic currents for the RDDE [24, 25] by representing solution/electrode interfaces as double-layer capacitors or charge-transfer resistors, respectively. We assumed the same double-layer capacitor, C_d, for symmetric CFMs (Figure 1B) or two different charge-transfer resistors, R_G and R_C at voltammetric generator and amperometric collector electrodes, respectively. The equivalent circuit is simplified by assuming a single current pathway between each CFM and a reference electrode as represented by a common resistance in the solution, R_S, and a solution resistance in the gap, R_{NG}. This assumption is approximate because only the interior side of a carbon fiber surface is exposed to a nanogap. We also

consider the resistance of carbon fiber, R_{CF}, [39] to define the non-common resistance of each electrode, R (= R_{NG} + R_{CF}).

It should also be noted that double CFMs represent an "open" nanogap cell, where two working electrodes are connected to a counter electrode to cause resistive coupling. By contrast, the resistive coupling is not expected for the "closed" nanogap cell based on two working electrodes without an additional counter or reference electrode. In the closed nanogap cell, the current response of one electrode must be opposite to that of the other electrode. The "closed" cells were used for the electrochemical detection of single molecules [7-9, 21] to cause capacitive coupling [10, 21, 22].

2.2. Non-Faradaic resistive coupling

We employed the equivalence circuit with double-layer capacitances (Figure 1B) to demonstrate that the non-Faradaic current response of the amperometric collector electrode varies with a change in the non-Faradaic current response of the voltammetric generator electrode at initial and switching potentials. The resultant current spikes were observed with double CFMs in our previous work [18] and are attributed to resistive coupling in this work. In our model, the potential of each electrode depends on the current response of both electrodes as given for the forward scan by

$$E_G = \frac{1}{C_d}\int_0^t i_G dt + (i_G + i_C)R_S + i_G R = E_i + vt \quad (1)$$

$$E_C = \frac{1}{C_d}\int_0^t i_C dt + (i_G + i_C)R_S + i_C R \quad (2)$$

where E_i is the initial potential, v is the potential scan rate, and E_C is constant against the reference electrode. Eqs 1 and 2 were combined to yield

$$I_G = \frac{i_G}{C_d v} = \frac{1}{2}\left\{2 - \exp\left[-\frac{t}{\left(1+{}^{2R_S}/_{R}\right)RC_d}\right] - \exp\left(-\frac{t}{RC_d}\right)\right\} \quad (3)$$

$$I_{\mathrm{C}} = \frac{i_{\mathrm{C}}}{C_{\mathrm{d}}v} = -\frac{1}{2}\left\{\exp\left[-\frac{t}{\left(1+{}^{2R_{\mathrm{S}}}/_{R}\right)RC_{\mathrm{d}}}\right] - \exp\left(-\frac{t}{RC_{\mathrm{d}}}\right)\right\} \quad (4)$$

where I_{G} and I_{C} represent normalized current responses of generator and collector electrodes, respectively. The polarity of the generator and collector responses were simply reversed during the reverse scan.

Eqs 3 and 4 were used to plot non-Faradaic generator and collector responses in the normalized forms (I_{G} and I_{C} in Figures 2A and B, respectively) while the scan of the generator potential was initiated at $t/RC_{\mathrm{d}} = 0$ and switched at $t/RC_{\mathrm{d}} = 10$. With $R_{\mathrm{S}}/R = 0.5$, the amperometric response of the collector electrode showed current spikes despite the fixed potential against the reference electrode when the potential of the generator electrode was scanned from initial and switching potentials. A current spike reflects a sudden change in the non-Faradaic current response of the generator electrode, which alters the common Ohmic potential drop and, subsequently, the potential drop across the interface between the collector electrode and the solution (Figure 1B). The corresponding non-Faradaic current response of the collector electrode increases and decays toward zero when the generator response reaches a steady state. The current spike of the amperometric collector electrode varies with R_{S}/R to reach the maximum value of $C_{\mathrm{d}}v/2$ with $R_{\mathrm{S}} >> R$. The non-Faradaic current response of the amperometric collector electrode is zero with $R_{\mathrm{S}}/R = 0$ owing to the lack of resistive coupling with the generator electrode. Resistive coupling also affects the generator response (Figure 2A), which also yields the standard non-Faradaic response of a voltammetric generator electrode with $R_{\mathrm{S}}/R = 0$ [40].

2.3. Faradaic resistive coupling

Resistive coupling results in the pseudocollection effect [24, 25] when Faradaic reactions are driven at both working electrodes. Faradaic resistive coupling is modeled by replacing double-layer

capacitors at generator and collector electrodes (Figure 1B) with charge-transfer resistors, R_G and R_C, respectively, to yield the corresponding electrode potentials given by

$$E_G = i_G R_G + (i_G + i_C)R_S + i_G R = E_i + vt \quad (5)$$

$$E_C = i_C R_C + (i_G + i_C)R_S + i_C R \quad (6)$$

where the non-Faradaic current was neglected for both electrodes. Eq 6 is equivalent to

$$i_C = \frac{E_C}{R_C + R_S + R} - \frac{i_G R_S}{R_C + R_S + R} \quad (7)$$

The first term on the right-hand side of eq 7 represents the intrinsic current response of the collector electrode. The second term represents the pseudo-collection effect owing to resistive coupling with the generator electrode [24, 25], where i_C appears as a mirror image of i_G when the second term is dominant. Eq 7 also indicates that the pseudocollection effect is enhanced when R_S becomes larger. Eventually, the second term on the right-hand side of eq 7 reaches $-i_G$ with $R_S >> R_C + R$. The pseudocollection effect diminishes without resistive coupling, i.e., $R_S = 0$.

3. Experimental Section

3.1. Chemicals and materials

$Ru(NH_3)_6Cl_3$ was obtained from Strem Chemicals (Newburyport, MA). L-ascorbic acid (AA), DA hydrochloride**,** 2-amino-2-(hydroxymethyl)-1,3-propanediol (Tris) hydrochloride were purchased from Sigma Aldrich (St. Louis, MO). A Milli-Q IQ 7003 water purification system (EMD Millipore, Billerica, MA) was used to obtain UV-treated deionized ultrapure water (18.2 MΩ·cm) with a total organic carbon value of 2–3 ppb as measured by using an internal online monitor. DA and AA were dissolved in the Tris buffer similar to cerebellum fluids containing 15 mM Tris hydrochloride, 140 mM NaCl, 3.25 mM KCl, 1.2 mM $CaCl_2$, 1.25 mM NaH_2PO_4, 1.2 mM $MgCl_2$ and 2.0 mM Na_2SO_4 at pH 7.4. Sample solutions were freshly prepared just before electrochemical experiments and were used

without removing the residual oxygen. No significant change in DA and AA responses was observed when the solution was purged with nitrogen [18].

3.2. Electrochemical measurement with modified bipotentiostat

A commercial bipotentiostat (CHI 7042D, CH Instruments, Austin TX) was modified (Figure 3) to compensate the collector potential, E_C, by the Ohmic potential drop based on the current response of the voltammetric generator electrode, i_G, and the solution resistance shared by the two electrodes, R_S. Specifically, the current response of the generator electrode was converted to the voltage signal, $-i_G R_1$, by the current follower, CF1, and the voltage subtractor, VS. Some fraction, f, of the output voltage signal was selected to feed the resultant voltage of $-i_G f R_1$ to the summing point of the feedback loop between the voltage subtractor and the potential control amplifier, PC. The resultant potential of the collector electrode against the reference electrode was equivalent to $E_C - i_G f R_G$. Resistive coupling was minimized when the fraction, f, was adjusted to yield $fR_1 = R_S$ (i.e., $i_G f R_G = i_G R_S$), which eliminated $i_G R_S$ from the colletor potential, $E_C - i_G f R_G$.

In addition, the circuit board was modified to control the generator potential through a fast parallel digital-to-analog converter (DAC) as reported previously [18]. The generator electrode was connected to the bipotentiostat as the secondary working electrode to cycle its potential against a Ag/AgCl electrode (CHI 111, CH Instruments) as a reference/counter electrode. A slow serial DAC was used to control the potential of the collector electrode, which was virtually grounded and biased at a constant potential against the reference electrode. Software and firmware were also modified accordingly.

4. Results and Discussion

4.1. Non-Faradaic resistive coupling

We investigated the resistive coupling of non-Faradaic current responses between double CFMs (Figure 1A) by considering the equivalent circuit based on two double-layer capacitors (Figure 1B). Double CFMs were separated by an ~150 nm-wide gap [18] and immersed in 1 M KCl. The potential of a voltammetric generator electrode was cycled to obtain a non-Faradaic current response, which varied with the scan rate (100 V/s; black line in Figure 4A). The potential of an amperometric collector electrode was set at 0.07 V, which did not drive any redox reaction. The resultant current response of the amperometric collector electrode spiked at the initial and switching potentials of the voltammetric generator electrode (black solid line in Figure 4B) as observed previously [18] and predicted by using the equivalent circuit in this work (Figure 2B). More quantitatively, the equivalent circuit predicts similarly high current spikes with opposite polarities at initial and switching potentials. The experimental current spike, however, was higher at the switching potential than at the initial potential for the first potential cycle. This discrepancy is attributed to the delayed response of the bipotentiostat at the start of the potential cycle. For the continuous second potential cycle, the spike current response of the amperometric collector electrode at the initial potential of the generator electrode was as high as that at the switching potential (black dashed line in Figure 4B).

The current spikes at the amperometric collector electrode were suppressed by compensating the common Ohmic potential drop, $i_G R_S$, by using the modified bipotentiostat and, subsequently, are attributed to resistive coupling. Specifically, the modified bipotentiostat applies a potential of $E_C – i_G f R_1$ instead of E_C to the collector electrode against the reference electrode (Figure 3). The common Ohmic potential drop, $i_G R_S$, is eliminated from $E_C – i_G f R_1$ to suppress resistive coupling when $f R_1 = R_S$, i.e., $i_G f R_1 = i_G R_S$. The current spikes became negligible when the compensated resistance, $f R_1$, was adjusted to 8

kΩ (Figure 4C). The amperometric collector response was noisier with the compensation of the common Ohmic potential drop, which is attributed to the imperfect shielding of the modified circuit board of the bipotentiostat. The current response of the voltammetric generator electrode (i_G = ~200 nA as an average) was much higher than that of the amperometric collector electrode (i_C = ~10 nA at the spike) and was not noticeably affected by the compensation of the common Ohmic potential drop (red line in Figure 4A). The compensated common Ohmic potential drop is approximated to $i_G f R_1$ = 1.4 mV. This small Ohmic potential drop is substantial enough to cause noticeable resistive coupling and corresponding current spikes. The ratio of the current spike at the amperometric collector electrode to the average current at the generator electrode is 0.05, which corresponds to R_S/R = 0.2 in eq 4. This ratio with R_S = 8 kΩ corresponds to $R = R_{CF} + R_{NG}$ = 40 kΩ (Figure 1B), thereby yielding R_{NG} = ~30 kΩ in 1 M KCl when R_{CF} = ~10 kΩ [39].

It should be noted that resistive coupling was not suppressed simply by connecting double CFMs to different reference/counter electrodes in the same cell [29]. This result indicates that the current pathway shared by the two CFMs was localized near the nanogap. The two reference electrodes were connected to unbiased and biased potentiostats as we developed and validated for SECM-based nanogap cells [19], where resistive coupling was negligible owing to slow scan rates of up to 10 V/s.

4.2. Faradaic resistive coupling

Faradaic resistive coupling was observed by using double CFMs and suppressed by compensating the common Ohmic potential drop (Figure 5). Experimentally, $Ru(NH_3)_6^{3+}$ was reduced to $Ru(NH_3)_6^{2+}$ at the voltammetric generator electrode at the fast scan rate of 500 V/s and regenerated from $Ru(NH_3)_6^{2+}$ by the amperometric collector electrode at 0.07 V. The voltammogram of the generator electrode showed current peaks at –0.26 and –0.12 V during forward and reverse potential scans,

respectively (Figure 5A). The corresponding current peaks were also observed at the collector electrode when the common Ohmic potential drop was not compensated (black line in Figure 5B). A positive current peak at the collector electrode around –0.12 V is attributed to resistive coupling because only the $Ru(NH_3)_6^{2+}$ oxidation is driven at the collector electrode to yield a negative current in our definition. Current peaks at –0.26 and –0.12 V are similar in shape between generator and collector electrodes but are mirror-imaged to each other as reported for the pseudo-collection effect [24, 25] and expected from eq 7. In addition, high current spikes were observed at the collector electrode at the initial and switching potentials of the generator electrode and are attributed to resistive coupling. These current spikes are higher at 500 V/s than at 100 V/s (Figure 4B) as expected from eq 4.

The amperometric collector electrode yielded a steady-state voltammogram without current spikes except at the switching potential when the common Ohmic potential drop was compensated (red line in Figure 5B). The resultant current response of the collector electrode was Faradaic and is attributed to the steady-state redox cycling of the $Ru(NH_3)_6^{3+/2+}$ couple between the two electrodes as expected from voltammetric theory [17]. The adjusted fR_G value of 8 kΩ corresponds to the common Ohmic potential drop of $i_G R_S$ = ~10 mV for the highest current response of i_G = ~1.3 μA at the generator electrode. By contrast, a current spike at the switching potential was suppressed excessively to yield the opposite spike. The error is attributed to the delayed response of the potentiostat. This dealy was more noticeable at 500 V/s than at 100 V/s (Figure 4B) but was consistently ~10 μs at both scan rates. The bipotentiostat is delayed by the coupling of the feedback resistor (R_1 in Figure 3) with stray capacitance. Specifically, a feedback resistance of R_1 = 1 MΩ was used to measure the generator response of ~1 μA (Figure 5B). Stray capacitance, C_1, of 10 pF yields a time constant of R_1C_1 = ~10 μS, which corresponds to a noticeable change of 5 mV in the generator potential at 500 V/s. A smaller feedback resistance of 0.1 MΩ shortened the delay time, but yielded a smaller $i_G R_1$, which resulted in the extremely noisy

current at the amperometric collector electrode when the common Ohmic potential drop was compensated.

The fastest scan rate of 500 V/s in this work is 4,000 times faster than the scan rate of 0.13 V/s employed previously for the suppression of resistive coupling in RRDE by the compensation of the common Ohmic potential drop [26]. In the previous work, the electrodes were rotated at 2500 rpm to observe transient voltammetric responses to the underpotential deposition of hydrogen and surface oxidation at the disk Pt electrode. The scan rate of 0.13 V/s was fast enough to observe the pseudo-collection effect at the amperometric ring Pt electrode, where the potential was set to barely drive the hydrogen evolution reaction. The maximum value of the compensated Ohmic potential drop was 18 mV for the common resistance of 90 Ω and the maximum current response of 200 μA at the disk Pt electrode. The compensated potential drop in the previous work is similar to that in this work despite very different scan rates and cell configurations.

4.3. Dopamine detection without resistive coupling

We compensated the common Ohmic potential drop to investigate the intrinsic Faradaic response of the CFM to DA without resistive coupling. The potential of the generator electrode was scanned at 100 V/s to oxidize DA to DOQ, which was reduced by the amperometric collector electrode at a sufficiently negative potential of –0.5 V. The generator electrode yielded an ordinary surface wave with a pair of current peaks based on DA oxidation and DOQ reduction during forward and reverse scans, respectively [41] (0.28 and 0.01 V, respectively, in Figure 6A). Without the compensation, the corrector response was distorted by resistive coupling to yield current spikes around the peak potentials of DA oxidation and DOQ reduction at the generator electrode in addition to initial and switching potentials (Figure 6B). These spikes were eliminated by compensating the common Ohmic potential drop at the

collector electrode, which resulted in sigmoidal voltammetric responses (Figure 6C). The steady-state voltammograms are expected for the efficient redox cycling of the DA/DOQ couple across the nanogap between generator and collector electrodes from voltammetric theory [17]. The optimum fR_1 value of 30 kΩ in the Tris buffer with a lower ionic strength of ~0.1 M was larger than that of 8 kΩ in 1 M KCl (Figures 4B and 5B). The current spikes at initial and switching potentials were higher in the Tris buffer than in 1 M KCl (Figure 4B) when the same potential scan rate of 100 V/s was employed. This result indicates a higher R_S/R in the Tris buffer because the carbon fiber resistance, R_{CF}, is independent of the ionic strength in contrast to R_S and R_{NG} (Figure 1B) and included in R.

The suppression of resistive coupling also yielded the intrinsic Faradaic response to DA at the collector electrode in the presence of AA as a major interfering species in biological media [42]. We investigated generator and collector voltammograms of only AA in the Tris buffer (Figures 7A and 7B) and then a mixture of AA and DA (Figures 7C and 7D). AA was adsorbed on and oxidized at the carbon fiber surface as represented by a surface wave at the generator electrode during the forward scan (Figure 7A). The oxidized product, dehydroascorbic acid, was instantaneously hydrolyzed to a redox-inactive species [43] as evidenced by the lack of the generator response during the reverse scan. Since the final product was redox-inactive, the current response of the collector electrode was not expected when the generator electrode yielded a peak current response to AA around 0.15 V. The collector electrode, however, yielded the negative current peak followed by the positive current peak during the forward scan when the common Ohmic potential drop was not compensated (Figure 7B). The collector response resembled the current peak followed by the rise of the background current at the generator electrode (Figure 7A) as expected for the pseudo-collection effect based on resistive coupling from eq 7. By contrast, the collector electrode did not yield any current response during the oxidation of AA at the generator electrode when the common Ohmic potential drop was compensated (Figure 7C). The

elimination of AA interference through the suppression of resistive coupling is significant because AA affects the DA response of not only the generator electrode but also the collector electrode (Figures 7C and 7D, respectively). The oxidation of DA adsorbed on the generator electrode was preceded by AA oxidation and was slowed down by AA adsorption to yield a widely separated pair of current peaks at 0.64 and 0.14 V (Figure 7D). The peak potentials were also shifted positively by the competitive adsorption of AA in comparison with only DA in the solution (0.28 and 0.01 V in Figure 6A). Moreover, the generator responses to AA and DA were resistively coupled to yield the corresponding current peaks at the collector electrode (Figure 7E). Resistive coupling was suppressed by compensating the common Ohmic potential drop to observe the steady-state voltammogram based on the intrinsic collector response to DA (Figure 7F).

4.4. Dual pathways for DA oxidation

Here, we analyze and interpret the features of compensated voltammograms without resistive coupling (Figure 6) to manifest the dual oxidation pathways of DA in adsorbed and non-adsorbed forms. The dual pathways were proposed previously [36] and were observed in this work because the adsorption and desorption of DA and DOQ are negligibly slow during the potential cycle [41]. The respective adsorption steps are given by

$$DA \rightleftharpoons DA_{ads} \quad (8)$$

$$DOQ \rightleftharpoons DOQ_{ads} \quad (9)$$

During the forward scan, the voltammetric generator electrode oxidizes the adsorbed form of DA to the adsorbed form of DOQ, which is not desorbed from the electrode surface and is reduced to the adsorbed form of DA during the reverse scan as given by

$$DA_{ads} \rightleftharpoons DOQ_{ads} + 2H^+ + 2e \quad (10)$$

Eq 10 is confirmed by a pair of the corresponding adsorption peaks at the generator electrode (Figure 6A). By contrast, the collector electrode reduces the non-adsorbed form of DOQ to obtain a steady-state-diffusion voltammogram (Figure 6C). The non-adsorbed form of DOQ can not be obtained by the slow desorption of DOQ from the generator electrode surface because the desorption kinetics is too slow. The non-adsorbed form of DOQ must be obtained from the non-adsorbed form of DA at the generator electrode as given by

$$DA \rightleftharpoons DOQ + 2H^+ + 2e \quad (11)$$

Moreover, the reverse reaction of eq 11 was observed at the collector electrode, where the non-adsorbed form of DOQ must be reduced to the non-adsorbed form of DA to maintain redox cycling of the DA/DOQ couple between the generator and collector electrodes. DA was preadsorbed on the collector electrode but was not desorbed or adsorbed during the potential cycle owing to the slow adsorption/desorption kinetics.

The oxidation of DA to DOQ at the carbon-fiber electrode is mediated by the formation of an intermediate, dopamine semi-quinone (DSQ), through either non-concerted or concerted mechanisms [37, 38]. Electron-transfer and adsorption steps are separated in the non-concerted mechanism (Figure 8A), where the adsorbed form of DSQ is formed from the adsorbed form of DA and oxidized to the adsorbed form of DOQ at the generator electrode (red allows in Figure 8A). Similarly, the non-adsorbed form of DA is oxidized to the non-adsorbed form of DOQ through the non-adsorbed form of DSQ (blue allows in Figure 8A) at both generator and collector electrodes. By contrast, electron-transfer and adsorption steps are coupled in the concerted mechanism (Figure 8B) to oxidize the non-adsorbed form of DA to the non-adsorbed form of DOQ through the adsorbed form of DSQ at both generator and collector electrodes (purple allows in Figure 8B). Similarly, the adsorbed form of DA is oxidized to the adsorbed form of DOQ through the non-adsorbed form of DSQ at the generator electrode (green allows

in Figure 8B). The adsorption-coupled electron-transfer steps of the concerted mechanism are accelerated by the electrode potential [37, 38] to become sufficiently fast while the adsorption of DA and DOQ (eqs 8 and 9, respectively) is potential-independent and negligibly slow [41].

The non-concerted and concerted mechanisms of DA oxidation at the CFM can not be discriminated voltammetrically, because the intermediate, DSQ, is not detectable. The two mechanisms can be discriminated for a one-electron-transfer reaction when the electron-transfer reaction is chemically reversible and an adsorption step is kinetically controlled [19]. These two requirements are satisfied for DA oxidation. In addition, the adsorbed or non-adsorbed form of DSQ must be identified for discrimination between the two mechanisms because DA oxidation is a two-electron-transfer reaction. We employed the finite element simulation to demonstrate that the non-concerted and concerted mechanisms of two-electron-transfer reactions can be discriminated voltammetrically when the three requirements are satisfied [38]. Experimentally, double CFMs are advantageous for the identification of the intermediate, DSQ, which must be either adsorbed or non-adsorbed form at the collector electrode in the concerted or non-concerted mechanism, respectively (Figure 8). By contrast, both forms of DSQ are present at the generator electrode or a single CFM. DSQ, however, was not detectable voltammetrically at the collector electrode because the reduction of DSQ to DA is thermodynamically more favorable than the reduction of DOQ to DSQ [44]. Accordingly, DSQ is formed from DOQ but is immediately reduced to DA and is not detected.

It should be noted that the self-catalytic oxidation of non-adsorbed DA by adsorbed DOQ as a catalyst was proposed previously by assuming the non-concerted mechanism [36]. In the self-catalytic mechanism, the non-adsorbed form of DA is oxidized to the non-adsorbed form of DOQ by the adsorbed form of DOQ as given by

$$DA + DOQ_{ads} \rightleftharpoons DOQ + DA_{ads} \quad (12)$$

The adsorbed form of DA is produced from the adsorbed form of DOQ but is immediately reduced to the adsorbed form of DOQ by the underlying electrode to maintain the catalytic cycle. This mechanism was proposed to explain why non-adsorbed DA can not be oxidized when the electrode surface is modified with a blocking organic layer to eliminate adsorbed species. This phenomenon, however, can be also explained by the concerted mechanism, where the adsorbed form of DSQ must be formed as an intermediate but not as a catalyst (Figure 8B).

5. Conclusions

In this work, we suppressed resistive coupling between the generator and collector electrodes of the nanogap electrochemical cell to manifest intrinsic collector responses. This work is the first to suppress resistive coupling in nanogap or microgap cells. These gaps are too narrow to minimize the common solution resistance of the two electrodes by optimizing the position of a reference electrode, which was successful for the RDDE with a millimeter-wide gap [23-29]. Alternatively, we modified a commercial potentiostat to compensate the Ohmic potential drop through the common solution resistance. Previously, this approach was applied for the RDDE at slow scan rates of 50 mV/s, which were required to ensure diffusional crosstalk across the millimeter-wide gap [26]. In comparison, we were able to suppress resistive coupling at much faster scan rates of up to 500 V/s, where the accurate current measurement was limited by the response time of the bipotentiostat. This limitation will be overcome by implementing our approach into the bipotentiostat that is tailormade for fast-scan cyclic voltammetry of multi-analyte detection with double CFMs [20].

This work demonstrates the power of nanogap cells to advance our fundamental understanding of electrochemical sensing mechanisms as exemplified by DA oxidation. The suppression of resistive coupling between double CFMs unambiguously manifested dual pathways for DA oxidation, which

were proposed previously [36] but have not been observed separately. The dual oxidation mechanism implies that the non-adsorbed form of DA is oxidized and depleted in the solution near the CFM during fast-scan cyclic voltammetry although the corresponding current response is dominated by the oxidation of preadsorbed DA [41]. We also found that DA oxidation can be mediated through either a non-concerted or concerted mechanism while only the former mechanism was considered previously [36]. DA oxidation satisfies both requirements for the discrimination between the two mechanisms of one-electron transfer, which must be chemically reversible and kinetically limited by the adsorption step. The two mechanisms, however, can not be discriminated for DA oxidation, which does not satisfy the additional requirement found for two-electron-transfer reactions in this work, i.e., the detection of the first-oxidation product, DSQ. The reaction mechnaism must be identified to determine the thermodynamic and kinetic parameters of electron-transfer and adsorption steps [19].

6. Acknowledgment

S.A. acknowledges support from the National Institutes of Health (R01 GM112656) and the National Science Foundation (CHE-2304922). We also thank Dr. Peixin He (CH Instruments) and the electronics shop (University of Pittsburgh) for the modification of the bipotentiostat. S.-H.H. and D.C.J. acknowledge the Arts and Sciences Fellowships from the University of Pittsburgh.

7. References

[1] H.S. White, K. McKelvey, Redox cycling in nanogap electrochemical cells, Curr. Opin. Electrochem., 7(2018) 48–53.

[2] S. Amemiya, Nanoscale scanning electrochemical microscopy, in: A.J. Bard, C.G. Zoski (Eds.), Electroanalytical Chemistry, CRC Press2015, pp. 1-72.

[3] T. Kai, C.G. Zoski, A.J. Bard, Scanning electrochemical microscopy at the nanometer level, Chem. Commun., 54(2018) 1934–47.

[4] L. Rassaei, P.S. Singh, S.G. Lemay, Lithography-based nanoelectrochemistry, Anal. Chem., 83(2011) 3974–80.

[5] K. Fu, S.-R. Kwon, D. Han, P.W. Bohn, Single entity electrochemistry in nanopore electrode arrays: Ion transport meets electron transfer in confined geometries, Acc. Chem. Res., 53(2020) 719–28.

[6] S. Partel, C. Dincer, S. Kasemann, J. Kieninger, J. Edlinger, G. Urban, Lift-off free fabrication approach for periodic structures with tunable nanogaps for interdigitated electrode arrays, ACS Nano, 10(2016) 1086–92.

[7] F.-R.F. Fan, A.J. Bard, Electrochemical detection of single molecules, Science, 267(1995) 871–4.

[8] F.-R.F. Fan, J. Kwak, A.J. Bard, Single molecule electrochemistry, J. Am. Chem. Soc., 118(1996) 9669–75.

[9] K. Mathwig, T.J. Aartsma, G.W. Canters, S.G. Lemay, Nanoscale methods for single-molecule electrochemistry, Annu. Rev. Anal. Chem., 7(2014) 383–404.

[10] K. McKelvey, D.A. Robinson, N.J. Vitti, M.A. Edwards, H.S. White, Single Ag nanoparticle collisions within a dual-electrode micro-gap cell, Faraday Discuss., 210(2018) 189–200.

[11] K. Fu, D. Han, G.M. Crouch, S.-R. Kwon, P.W. Bohn, Voltage-gated nanoparticle transport and collisions in attoliter-volume nanopore electrode arrays, Small, 14(2018) 1703248.

[12] M.A.G. Zevenbergen, B.L. Wolfrum, E.D. Goluch, P.S. Singh, S.G. Lemay, Fast electron-transfer kinetics probed in nanofluidic channels, J. Am. Chem. Soc., 131(2009) 11471–7.

[13] S. Amemiya, Heterogeneous electron-transfer reactions, in: A.J. Bard, M.V. Mirkin (Eds.), Scanning Electrochemical Microscopy, 3rd ed., CRC Press, Boca Raton, FL, 2022, pp. 105–26.

[14] F.H. Cao, J. Kim, A.J. Bard, Detection of the short-lived cation radical intermediate in the electrochemical oxidation of *N*,*N*-dimethylaniline by scanning electrochemical microscopy, J. Am. Chem. Soc., 136(2014) 18163–9.

[15] T. Kai, M. Zhou, S. Johnson, H.S. Ahn, A.J. Bard, Direct observation of $C_2O_4^{\bullet-}$ and $CO_2^{\bullet-}$ by oxidation of oxalate within nanogap of scanning electrochemical microscope, J. Am. Chem. Soc., 140(2018) 16178–83.

[16] K. Fu, D. Han, C. Ma, P.W. Bohn, Electrochemistry at single molecule occupancy in nanopore-confined recessed ring-disk electrode arrays, Faraday Discuss., 193(2016) 51–64.

[17] P. Pathirathna, R.J. Balla, S. Amemiya, Simulation of fast-scan nanogap voltammetry at double-cylinder ultramicroelectrodes, J. Electrochem. Soc., 165(2018) G3026–G32.

[18] P. Pathirathna, R.J. Balla, S. Amemiya, Nanogap-based electrochemical measurements at double-carbon-fiber ultramicroelectrodes, Anal. Chem., 90(2018) 11746–50.

[19] N. Kurapati, D.C. Janda, R.J. Balla, S.-H. Huang, K.C. Leonard, S. Amemiya, Nanogap-resolved adsorption-coupled electron transfer by scanning electrochemical microscopy: Implications for electrocatalysis, Anal. Chem., 94(2022) 17956–63.

[20] N. Manring, M. Strini, J.L. Smeltz, P. Pathirathna, Simultaneous detection of neurotransmitters and Cu^{2+} using double-bore carbon fiber microelectrodes via fast-scan cyclic voltammetry, RSC Adv., 13(2023) 33844–51.

[21] P. Sun, M.V. Mirkin, Electrochemistry of individual molecules in zeptoliter volumes, J. Am. Chem. Soc., 130(2008) 8241–50.

[22] S.W. Feldberg, M.A. Edwards, Current response for a single redox moiety trapped in a closed generator-collector system: The role of capacitive coupling, Anal. Chem., 87(2015) 3778–83.

[23] C. Gabrielli, M. Keddam, H. Takenouti, Étude de la répartition du potentiel a la surface d'une électrode à disque-anneau, J. Chim. Phys., 69(1972) 737–40.

[24] M. Shabrang, S. Bruckenstein, Equivalent circuit for the uncompensated resistances occurring at ring-disk electrodes, J. Electrochem. Soc., 121(1974) 1439–44.

[25] M. Shabrang, Equivalent circuit for ring-disk electrode, J. Electrochem. Soc., 121(1974) 50C–4C.

[26] M. Shabrang, S. Bruckenstein, Compensation of Ohmic potential interactions occurring at ring-disk electrodes, J. Electrochem. Soc., 122(1975) 1305–11.

[27] C. Dörfeel, D. Rahner, W. Forker, Studies of coupling effects and ohmic potential drops at ring-disc electrodes, J. Electroanal. Chem. Interfacial Electrochem., 107(1980) 257–70.

[28] S. Vesztergom, N. Barankai, N. Kovács, M. Ujvári, P. Broekmann, H. Siegenthaler, G. G. Láng, Electrical cross-talk in rotating ring–disk experiments, Electrochem Commun., 68(2016) 54–8.

[29] S. Vesztergom, N. Barankai, N. Kovács, M. Ujvári, H. Siegenthaler, P. Broekmann, G. G. Láng, Electrical cross-talk in four-electrode experiments, J. Solid State Electrochem., 20(2016) 3165–77.

[30] A.J. Bard, F.-R.F. Fan, J. Kwak, O. Lev, Scanning electrochemical microscopy. Introduction and principles, Anal Chem, 61(1989) 132–8.

[31] D. Trinh, E. Maisonhaute, V. Vivier, Electrical cross-talk in transient mode of scanning electrochemical microscopy, Electrochem. Commun., 16(2012) 49–52.

[32] Z.J. Barton, J. Hui, N.B. Schorr, J. Rodríguez-López, Detecting potassium ion gradients at a model graphitic interface, Electrochim. Acta, 241(2017) 98–105.

[33] G. Zhang, Y. Cui, A. Kucernak, Real-time in situ monitoring of CO_2 electroreduction in the liquid and gas phases by coupled mass spectrometry and localized electrochemistry, ACS Catalysis, 12(2022) 6180–90.

[34] A.J. Bard, L.R. Faulkner, H.S. White, Electrochemical Methods: Fundamentals and Applications, 3rd ed., New York: John Wiley & Sons; 2022, pp. 740–4.

[35] B.J. Venton, Q. Cao, Fundamentals of fast-scan cyclic voltammetry for dopamine detection, Analyst, 145(2020) 1158–68.

[36] S.H. DuVall, R.L. McCreery, Self-catalysis by catechols and quinones during heterogeneous electron transfer at carbon electrodes, J. Am. Chem. Soc., 122(2000) 6759–64.

[37] O.V. Klymenko, I. Svir, C. Amatore, Molecular electrochemistry and electrocatalysis: a dynamic view, Mol. Phys., 112(2014) 1273–83.

[38] D.C. Janda, K. Barma, N. Kurapati, O.V. Klymenko, A. Oleinick, I. Svir, C. Amatore, S. Amemiya, Systematic assessment of adsorption-coupled electron transfer toward voltammetric discrimination between concerted and non-concerted mechanisms, Electrochim. Acta, 428(2022) 140912.

[39] C.J. Meunier, J.D. Denison, G.S. McCarty, L.A. Sombers, Interpreting dynamic interfacial changes at carbon fiber microelectrodes using electrochemical impedance spectroscopy, Langmuir, 36(2020) 4214–23.

[40] A.J. Bard, L.R. Faulkner, H.S. White, Electrochemical Methods: Fundamentals and Applications, 3rd ed., New York: John Wiley & Sons; 2022, pp. 48–50.

[41] B.D. Bath, D.J. Michael, B.J. Trafton, J.D. Joseph, P.L. Runnels, R.M. Wightman, Subsecond adsorption and desorption of dopamine at carbon-fiber microelectrodes, Anal. Chem., 72(2000) 5994–6002.

[42] D.L. Robinson, A. Hermans, A.T. Seipel, R.M. Wightman, Monitoring rapid chemical communication in the brain, Chem. Rev., 108(2008) 2554–84.

[43] P. Karabinas, D. Jannakoudakis, Kinetic parameters and mechanism of the electrochemical oxidation of L-ascorbic acid on platinum electrodes in acid solutions, J. Electroanal. Chem. Interfacial Electrochem., 160(1984) 159-67.

[44] C. Lin, L. Chen, E.E.L. Tanner, R.G. Compton, Electroanalytical study of dopamine oxidation on carbon electrodes: from the macro- to the micro-scale, Phys. Chem. Chem. Phys., 20(2018) 148–57.

Figure Captions

Figure 1. (A) SEM image of a double CFM and (B) the corresponding equivalent circuit of a nanogap electrochemical cell. R_{NG} and R_{CF} represent the resistances of the solution in the nanogap and the carbon fiber, respectively. The double-layer capacitance, C_d, is considered for non-Faradaic resistive coupling and replaced with charge transfer resistances for Faradaic resistive coupling. See text for other symbols.

Figure 2. Non-Faradaic current responses of (A) voltammetric generator and (B) amperometric collector electrodes as calculated by using eqs 3 and 4, respectively.

Figure 3. Scheme of bipotentiostat circuit with generator, collector, and reference/counter electrodes in the electrochemical cell (circle) for the positive feedback compensation of the common Ohmic potential drop, $-i_G f R_1$ ($= -i_G R_S$), at the collector electrode.

Figure 4. Non-Faradaic (A) generator and (B) and (C) collector responses of double CFMs in 1 M KCl with and without compensation of R_S = 8 kΩ. The generator potential was scanned from 0.07 V to –0.43 V at 100 V/s. The collector potential was set at 0.07 V. The electrode potentials were measured against a Ag/AgCl reference electrode in 3 M KCl.

Figure 5. (A) Generator and (B) collector responses of double CFMs to 0.5 mM $Ru(NH_3)_6Cl_3$ in 1 M KCl with and without compensation of R_S = 8 kΩ. The generator potential was scanned from 0.07 V to –0.43 V at 500 V/s. The collector potential was set at 0.07 V. The electrode potentials were measured against a Ag/AgCl reference electrode in 3 M KCl.

Figure 6. (A) Generator and (B) and (C) collector responses of double CFMs to 0.1 mM DA in Tris at pH 7.4 with and without compensation of R_S = 35 kΩ. The generator potential was scanned from –0.5 V to 1.0 V at 100 V/s. The collector potential was set at –0.5 V. The electrode potentials were measured against a Ag/AgCl reference electrode in 3 M KCl.

Figure 7. (A) and (D) Generator and (B), (C), (E), and (F) collector responses of double CFMs to 5 mM AA without (A)–(C) and with (D)–(F) 0.1 mM DA in Tris at pH 7.4 with and without compensation of R_S = 35 kΩ. The generator potential was scanned from –0.5 V to 1.0 V at 100 V/s. The collector potential was set at –0.5 V. The electrode potentials were measured against a Ag/AgCl reference electrode in 3 M KCl.

Figure 8. DA oxidation through (A) non-concerted and (B) concerted mechanisms at generator (G) and collector (C) electrodes. Red and blue arrows indicate electron transfer separated from adsorption steps. Purple and green arrows indicate adsorption-coupled electron transfer. Black arrows indicate diffusion.

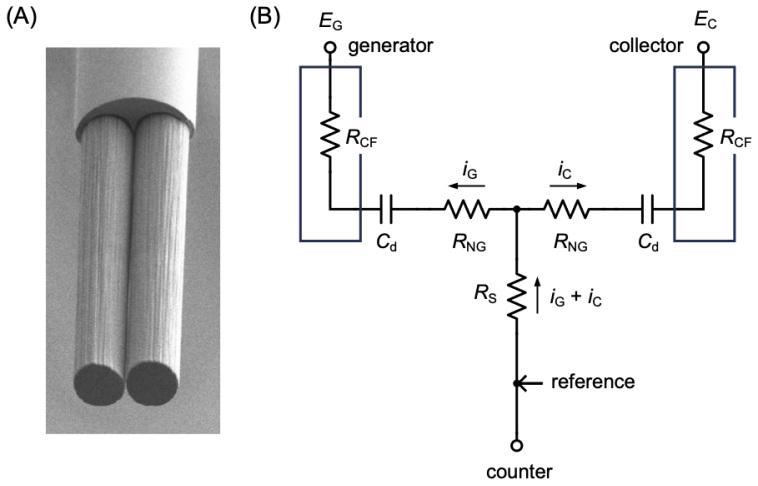
(A)
(B)
E_G
generator
E_C
collector
R_{CF}
R_{CF}
i_G
i_C
C_d
R_{NG}
R_{NG}
C_d
R_S
$i_G + i_C$
reference
counter

Figure 1

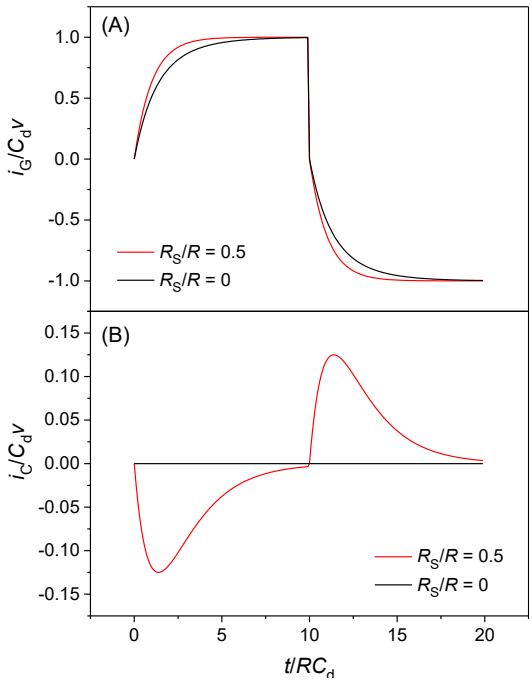
(A)
1.0
0.5
0.0
-0.5
-1.0
i_G/C_dv
$R_S/R = 0.5$
$R_S/R = 0$
(B)
0.15
0.10
0.05
0.00
-0.05
-0.10
-0.15
i_C/C_dv
$R_S/R = 0.5$
$R_S/R = 0$
0
5
10
15
20
t/RC_d

Figure 2

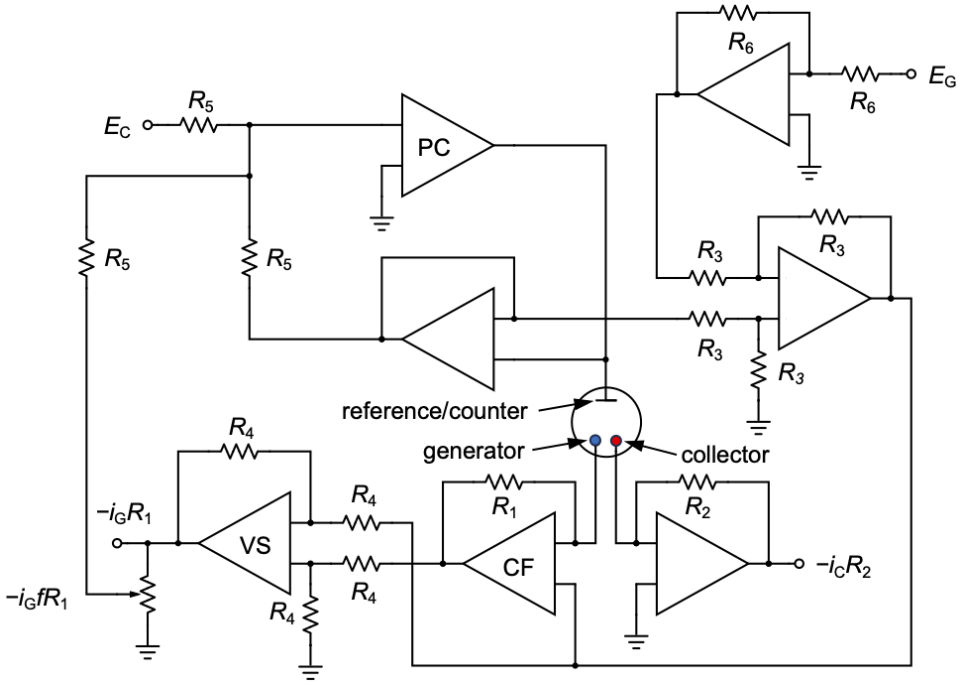
R_6
E_G
R_6
R_5
E_C
PC
R_5
R_5
R_3
R_3
R_3
R_3
reference/counter
generator
collector
R_4
R_1
R_2
$-i_G R_1$
R_4
VS
CF
$-i_C R_2$
$-i_G f R_1$
R_4
R_4

Figure 3

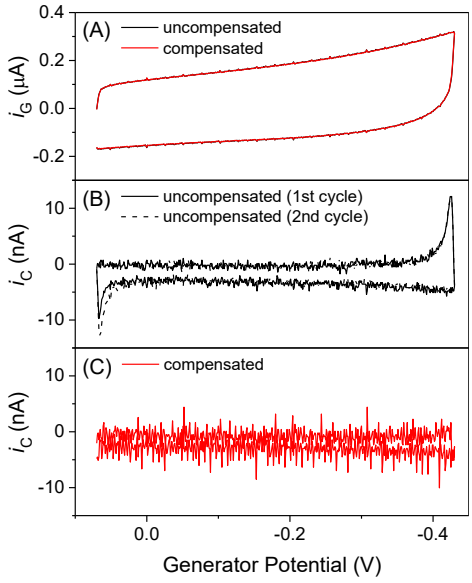
(A)
uncompensated
compensated
i_G (μA)
0.4
0.2
0.0
-0.2
(B)
uncompensated (1st cycle)
uncompensated (2nd cycle)
i_C (nA)
10
0
-10
(C)
compensated
i_C (nA)
10
0
-10
0.0
-0.2
-0.4
Generator Potential (V)

Figure 4

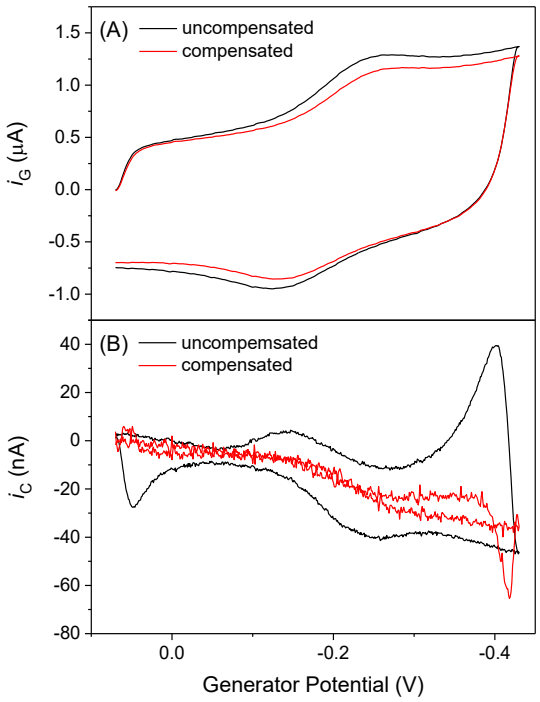
(A)
uncompensated
compensated
1.5
1.0
0.5
0.0
-0.5
-1.0
i_G (μA)
(B)
uncompemsated
compensated
40
20
0
-20
-40
-60
-80
i_C (nA)
0.0
-0.2
-0.4
Generator Potential (V)

Figure 5

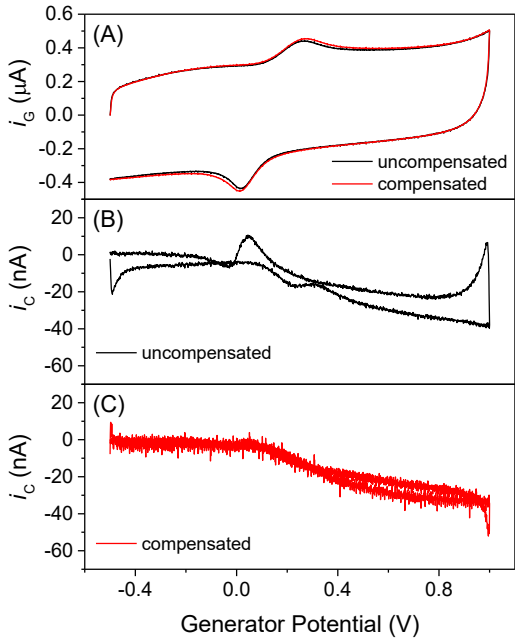
(A)
(B)
(C)
i_G (μA)
i_C (nA)
i_C (nA)
uncompensated
compensated
uncompensated
compensated
0.6
0.4
0.2
0.0
-0.2
-0.4
20
0
-20
-40
-60
-0.4
0.0
0.4
0.8
Generator Potential (V)

Figure 6

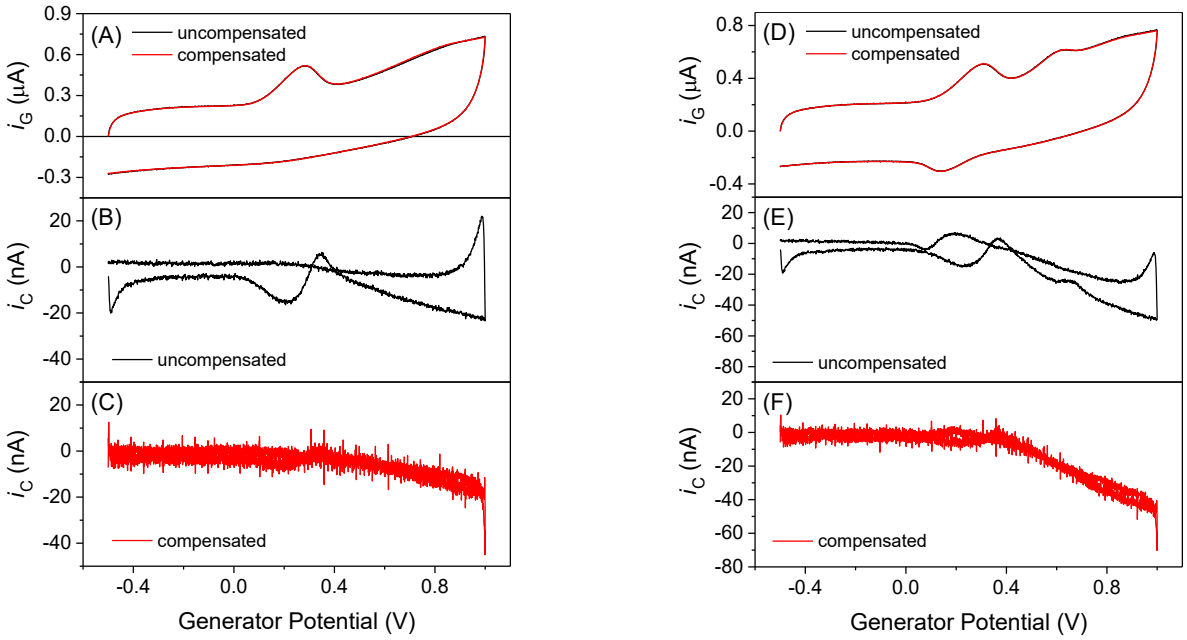
(A)
uncompensated
compensated
i_G (μA)
(B)
i_C (nA)
uncompensated
(C)
i_C (nA)
compensated
Generator Potential (V)
(D)
uncompensated
compensated
i_G (μA)
(E)
i_C (nA)
uncompensated
(F)
i_C (nA)
compensated
Generator Potential (V)

Figure 7

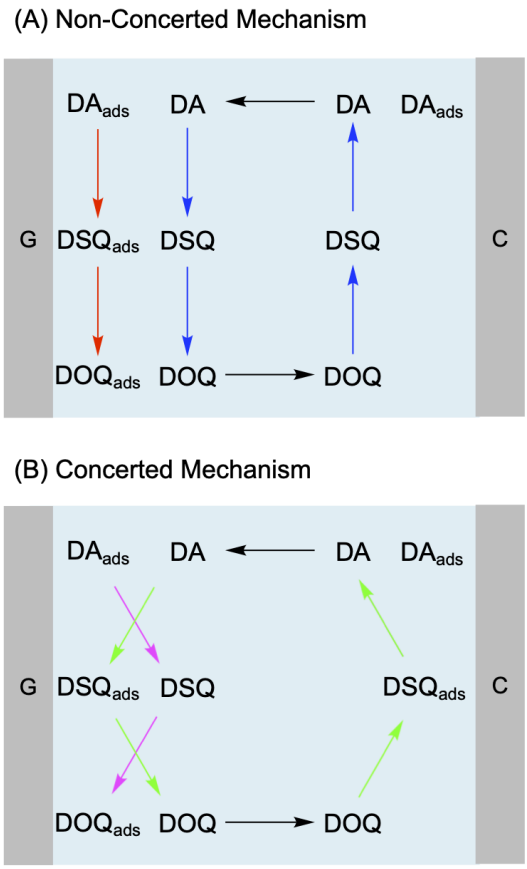
(A) Non-Concerted Mechanism
G
C
DA_ads
DA
DA
DA_ads
DSQ_ads
DSQ
DSQ
DOQ_ads
DOQ
DOQ
(B) Concerted Mechanism
G
C
DA_ads
DA
DA
DA_ads
DSQ_ads
DSQ
DSQ_ads
DOQ_ads
DOQ
DOQ

Figure 8